Integrin conformation-dependent neutrophil slowing obstructs the capillaries of the pre-metastatic lung in a model of breast cancer

Frédéric Fercoq[1,2#], Gemma S. Cairns[1#], Marco De Donatis[1,3], John B. G. Mackey[1], Alessia Floerchinger[1,4], Amanda McFarlane[1], Ximena L. Raffo-Iraolagoitia[1,3], Declan Whyte[1], Lindsey W. G. Arnott[1,3], Colin Nixon[1], Robert Wiesheu[1,3], Anna Kilbey[1,3], Leah Brown[1], Sarwah Al-Khalidi[1], Jim C. Norman[1,3], Edward W. Roberts[1,3], Karen Blyth[1,3], Seth B. Coffelt[1,3], Leo M. Carlin[1,3]*.

[1]Cancer Research UK Scotland Institute, Garscube Estate, Switchback Road, Glasgow, G61 1BD, UK

[2]Unit Communication Molecules and Adaptation of Micro-organisms (MCAM, UMR 7245), Team Parasites and Free Protistes, Muséum National d'Histoire Naturelle, CNRS; CP52, 61 rue Buffon, 75005 Paris, France

[3]School of Cancer Sciences, University of Glasgow, Garscube Estate, Switchback Road, Glasgow, G61 1QH, UK

[4]Faculty of Biosciences, University of Heidelberg, Germany.

[#]Joint first authors

*Correspondence to: Leo M. Carlin, Cancer Research UK Scotland Institute, Glasgow G61 1BD, email: leo.carlin@glasgow.ac.uk

Abstract

Neutrophils are thought to be critical to the process whereby breast cancers establish an immunosuppressive and tumour cell nurturing 'pre-metastatic' niche before overt metastasis can be detected. However, the spatial localization of neutrophils and their interaction with other cell types in the lung pre-metastatic niche is not well described. We used a spontaneously metastatic mammary cancer model combined with a multiplexed three- and four- dimensional imaging approach to investigate the behaviour of neutrophils in the pre-metastatic niche. Volume fixed tissue three-dimensional imaging showed that approximately 40% of $CD8^+$ T cells are adjacent to neutrophils at this stage. In live tissue, we found neutrophils with impaired intravascular motility congested the capillaries of pre-metastatic lungs potentially obstructing $CD8^+$ T cells. Slowed neutrophil transit was dependent on the conformation of β_2-integrin and could be recapitulated by treating non-tumour bearing mice with G-CSF, a potent systemic mediator of granulopoiesis. We found a decrease in L-selectin (CD62L) on neutrophils in the lungs of both mammary tumour bearing and G-CSF treated mice. Finally, we observed differential accumulation of intravenously injected micro-beads in the lung, suggestive of transient circulatory dead spaces which were also dependent on β_2-integrin inactivation. Overall, our study proposes that integrin-mediated neutrophil congestion of the alveolar capillaries could contribute to the generation of the pulmonary pre-metastatic niche.

40 ## Introduction

41 Neutrophils have been linked to both pro- and anti-tumour activity based on stage and context[1]
42 and have been mechanistically implicated in promoting breast cancer metastasis[2–4]. Tumours
43 are known to affect their eventual site of metastasis, even before overt metastasis is detected,
44 forming an environment termed the pre-metastatic niche[5]. Several single cell technologies
45 have been brought to bear on the metastatic and pre-metastatic environment yielding
46 important data on the heterogeneity and plasticity of neutrophils in cancer, but this information
47 often lacks direct spatiotemporal information[6]. Tumours spread to the lung in approximately
48 30% of metastatic breast cancer patients[7,8] and these patients have much poorer outcomes[9].
49 The lung is a unique physiological barrier with a need for carefully balanced regulation
50 between robust immune response and tissue damage. This balance is thought to err on the
51 side of immunosuppression, resolution, and containment to avoid life threatening
52 inflammation[10]. This, along with the extensive narrow vasculature acting as a filter or strainer,
53 makes the lung a key site for metastatic seeding and outgrowth.

54 Therefore, we probed the behaviour of neutrophils within the lungs of mice bearing
55 spontaneously lung metastatic mammary tumours at a stage before overt lung metastasis
56 could be observed. Using a combination of cleared, fixed, and live *ex vivo* three- and four-
57 dimensional multiplexed immunofluorescence imaging of lung slices we found that the
58 pulmonary capillaries were packed with neutrophils in tumour bearing mice. $CD8^+$ T cells
59 within this environment were almost unavoidably in close contact with the neutrophils. Live
60 imaging revealed that the neutrophils moved more slowly than their counterparts in the lungs
61 of healthy mice. This change in neutrophil migratory phenotype was dependent on β_2-integrin
62 conformation, a key determinant of neutrophil:endothelium interactions[11], and was
63 recapitulated by G-CSF treatment in non-tumour bearing mice. Expression of cell surface L-
64 selectin (CD62L), a leukocyte adhesion molecule known to induce β_2-integrin activation on
65 neutrophils[12], was reduced on the surface of lung neutrophils in both mammary tumour
66 bearing, and G-CSF treated mice. We speculate that this aberrant neutrophil intravascular
67 motility is a by-product of phenotypically modified neutrophils from stress granulopoiesis
68 stimulated in part by G-CSF produced by the tumour microenvironment. We suggest that these
69 results are important to consider when targeting T cells or neutrophils in the pre-metastatic
70 niche.

71

72

73

74 ## Results and discussion

75 **'Pre-metastatic' lung capillaries are neutrophilic**

76 To interrogate the lung pre-metastatic niche we used a murine model of metastatic breast
77 cancer, where either female FVB/N mice, or Catchup$^{IVM\text{-}red}$ Ly6G neutrophil reporter mice[13],
78 were orthotopically transplanted with mammary tumour fragments from *K14-Cre;Trp53$^{F/F}$* (KP)
79 mice[14] (**Figure 1A**). As in the *K14-Cre;Cdh1$^{F/F}$;Trp53$^{F/F}$* (KEP) transplant model[2], tumour
80 resection before the mice reach humane endpoint allows them to subsequently develop lung
81 metastases with complete penetrance (**Figure S1**). Therefore, prior to resection, the lungs of
82 these mice recapitulate the pre-overt metastasis microenvironment.

83 In our KP transplant model, we confirmed using flow cytometry, the presence of significant
84 neutrophilia in the pre-metastatic lung of mice with 10-15 mm orthotopic KP mammary tumours
85 (2-6 weeks after transplant, usually week 4) (**Figure 1B, 1C and S2A**), which has been
86 previously reported for the KEP mammary tumour transplant model[2,15] and other metastatic
87 breast cancer models such as MMTV-PyMT[3] or 4T1[4,16]. As we previously found in other
88 metastatic models[17], neutrophilia was accompanied by an increase in both number and
89 percentage of immature Ly6G intermediate (Ly6G^{int}) neutrophils (**Figure 1D, 1E and S2B**).

90 Neutrophils and their interaction with T cells have been implicated in breast cancer lung
91 metastasis[2], however, little is known about the location and interactions of these two cell
92 populations in the pre-metastatic lung. Thus, we used chemically cleared precision-cut lung
93 slices (PCLS) to investigate the immune landscape in the pre-metastatic lung in three
94 dimensions (3D). Spectral multiplexed immunofluorescence confocal microscopy was
95 employed to identify immune cells using six markers simultaneously in large tissue volumes
96 while preserving tissue architecture and unmixing the lungs intrinsic autofluorescence
97 (**Figures 1F and S2C**). Consistent with flow cytometry, histocytometry[18,19] of 3D multiplexed
98 images demonstrated a substantial accumulation of neutrophils in the lungs of mice with 10-
99 15 mm orthotopic KP mammary tumours, with no statistically significant increase in CD68^{+}
100 macrophage or CD8^{+} T cell abundance (**Figures 1G, 1H**).

101 Most neutrophils and CD3^{+} T cells were found within the lung vasculature, particularly in
102 pulmonary capillaries and arteries (**Figure 1I and 1J**). We wondered whether the more
103 abundant neutrophils might use the lymphatics to reach the lymph nodes and influence T cells
104 there, but neutrophils were absent from the lymphatic collectors clearly apparent in podoplanin
105 stained sections (**Figure S3A**). Macrophages were predominantly localized in alveoli (alveolar
106 macrophages) or perivascular adventitial spaces (interstitial macrophages) (**Figure 1J)**. In

107 contrast with controls, approximately 40% of $CD8^+$ T cells were directly adjacent to neutrophils
108 in tumour bearing mice (**Figure 1J and 1K**) consistent with cell-cell interactions. Notably, the
109 proportion of T cells in contact with neutrophils correlated with the number of lung neutrophils
110 present (Spearman r = 0.8333 p=0.0083) (**Figure S3B**), suggesting that these interactions
111 might be primarily mediated by the significantly increased abundance of neutrophils.

112 Collectively, these findings indicate that the pre-metastatic pulmonary capillaries are
113 congested with neutrophils. This marked expansion in intravascular neutrophils may facilitate
114 unavoidable contact between neutrophils and $CD8^+$ T cells *in vivo.*

115 **Lung neutrophils do not produce oxidative burst in live PCLS from mammary tumour**
116 **bearing mice**

117 There is accumulating evidence that upon arrival in the lung, neutrophils acquire unique
118 immunosuppressive capacity to avoid damaging the delicate alveolar tree[4,20,21]. This capacity
119 is thought to be amplified in the context of tumour-driven inflammation[2,4]. Previous work
120 suggested that neutrophils could inhibit cytotoxicity of $CD8^+$ T cells in the lung through nitric
121 oxide[2]. We therefore imaged nitric oxide (NO) and superoxide (O_2^-) in live *ex vivo* PCLS to
122 investigate oxidative stress in neutrophils (as depicted in **Figures 2A and S4**). To check the
123 validity of the probes in neutrophils, we stimulated live PCLS with phorbol myristate acetate
124 (PMA) and saw expression of both NO and O_2^- in neutrophils and surrounding tissue (**Figures**
125 **S4A and S4D-E**). However, neither NO, nor O_2^- were detected in lung neutrophils in PCLS
126 from control or KP transplant tumour-bearing mice suggesting that this enhanced neutrophil
127 oxidative burst does not take place in the lungs at this timepoint (**Figures S4B-E**).

128 **Neutrophil motility is impaired in a CD18/ICAM-1 dependent manner in the pre-**
129 **metastatic lung**

130 Further investigation of live PCLS however revealed changes in neutrophil motility in lungs
131 from KP transplant tumour-bearing mice compared to controls. The neutrophils from KP
132 tumour-bearing mice exhibited shorter tracks and reduced mean track speeds compared to
133 those from control mice (**Figures 2B, 2C and Video S1**), while $CD8^+$ T cells were mostly
134 immotile in both groups (**Figure S4F**). Therefore, we investigated the mechanisms which
135 control intravascular neutrophil motility in the pre-metastatic lung. Imaging studies have
136 uncovered several examples where the endpoint of leukocyte (including neutrophil):
137 endothelial interactions is not extravasation into the tissue but rather intravascular motility or
138 'patrolling'[22–24]. In addition to selectins, neutrophil β_2-integrins, Mac-1 (CD11b/CD18; $\alpha_m\beta_2$)
139 and LFA-1 (CD11a/CD18; $\alpha_L\beta_2$), which bind to ICAM-1 (CD54) on endothelial cells are thought

140 to mediate neutrophil: endothelial cell interactions[11]. However, due to the narrow diameter of
141 lung capillaries, the typical neutrophil adhesion cascade does not occur. Instead, neutrophils
142 are forced into contact with the endothelium by constriction (**Figures 1I and 1J**).
143 Consequently, it has been postulated that integrins may not be essential for neutrophil
144 recruitment in the lung[25–27]. However, recent studies have suggested a requirement for CD11b
145 (Mac-1) in neutrophil intravascular motility[28], although it is likely that this regulation extends
146 beyond protein expression, as conformation and intracellular trafficking are known to regulate
147 integrin mediated binding.

148 Considering the above, we hypothesised that neutrophil intravascular motility in the lungs
149 could be attenuated by integrin inactivation. CD18 (β_2), the common beta-chain for both Mac-
150 1 and LFA-1, is expressed by neutrophils at similar levels in both controls and tumour bearing
151 mice (**Figure 2D and S2B**). As integrins undergo conformational changes that govern their
152 adhesion (e.g. to ICAM-1[11] on the endothelium; **Figure 2E**), we used three monoclonal
153 antibodies to manipulate CD18-ICAM-1 interactions in the lung to investigate this putative
154 mechanism (**Figure 2E**): (1) The CD18 activating antibody (clone M18/2) stabilises the active
155 conformation of CD18, promoting adhesion to ICAM-1[29]; (2) The clone GAME-46 blocks the
156 active domain of CD18, preventing adhesion to ICAM-1[29]; and (3) The ICAM-1 blocking
157 antibody (clone YN1/1.7.4) was used to block ICAM-1. Intravenous injection of tumour cells
158 has been shown to acutely increase neutrophil numbers in lung capillaries[30], recapitulating
159 that aspect of the pre-metastatic niche in an otherwise unaltered lung environment. We
160 intravenously injected a suspension of KP primary tumour cells plus GAME-46, M18/2, or
161 isotype control antibodies, and lungs were collected 30 minutes later (**Figure 2F**).
162 Subsequently, neutrophils were investigated by immunohistochemistry (IHC) for Ly6G in fixed
163 lung tissue to quantify neutrophil numbers, and in live PCLS to quantify neutrophil speed
164 (**Figures 2G and 2H**). Notably, there was no difference in neutrophil numbers in the lungs
165 across the different treatment groups (**Figures 2G and 2I**). However, CD18 blocking with
166 GAME-46 reduced neutrophil speed, whereas M18/2 increased neutrophil speed compared
167 to isotype control (**Figures 2H and 2J, Video S2**). Likewise, intravenous injection of KP
168 tumour cells with ICAM-1 blocking antibodies or isotype control did not impact neutrophil
169 numbers but blocking ICAM-1 inhibited neutrophil movement in live PCLS (**Figure S5**).

170 These results suggest that β_2-integrin conformation could be a critical modulator of neutrophil
171 motility in the pre-metastatic lung mediated by the primary tumour. Therefore, to investigate
172 whether CD18 conformational stabilisation altered neutrophil speed in the lungs of mice with
173 distant orthotopic KP tumours, we treated live PCLS from control and KP transplant tumour-
174 bearing mice with M18/2 *ex vivo* (**Figure 2K**). Antibody treatment had no significant impact on

175 neutrophil motility in control PCLS; however, M18/2 was able to restore neutrophil crawling
176 speed in PCLS from tumour-bearing mice (**Figures 2L, 2M and S6A**). This suggests that
177 tumour-driven neutrophil motility impairment could be mediated in part by conformational
178 inactivation of CD18.

179 **G-CSF recapitulates decreased lung neutrophil motility**

180 We next investigated the potential mediators of CD18 conformational change. It is known that
181 breast cancers induce neutrophilia through G-CSF[2–4]. We therefore wanted to probe whether
182 G-CSF could drive the neutrophil slowing we had observed in the tumour-bearing mice in the
183 absence of a tumour. Mice were administered a single 5 µg dose of G-CSF intraperitoneally,
184 and the lungs were collected 24 hours later to analyse neutrophil motility in *ex vivo* live PCLS,
185 and neutrophil abundance by IHC and flow cytometry (**Figure 3A**). In live PCLS, neutrophil
186 behaviour recapitulated that observed in tumour-bearing mice (**Figures 3B, 3C and 2M**).
187 Notably, neutrophil speed was reduced in G-CSF-treated mice, which could be rescued with
188 M18/2 as before (**Figures 3B, 3C and S6B**). As expected, lung neutrophil numbers were
189 substantially significantly increased following G-CSF treatment (**Figures 3D, 3E and 3F**), with
190 a trend for increased absolute number ($p=0.07$) and significantly increased ($p\leq0.001$)
191 percentage of $Ly6G^{int}$ neutrophils (**Figure 3F and 3G**). In line with the appearance of immature
192 neutrophils, CD101, which has been used as a neutrophil maturity marker in other cancer
193 models[31], decreased by approximately 50% with G-CSF treatment (**Figures 3H and 3I**) and
194 more moderately by approximately 20% in the tumour-bearing mice (**Figures 3J and 3K**).

195 **Reduced CD62L cell surface expression in lung neutrophils from G-CSF treated and KP**
196 **mammary tumour bearing mice.**

197 Interestingly, further immunophenotyping of lung neutrophils by flow cytometry (**Figure S2B**)
198 revealed that the level of cell surface CD62L was reduced in both G-CSF treated (**Figure 3L**
199 **and 3M**) and KP mammary tumour-bearing mice (**Figure 3N and 3O**). Interestingly, $CD62L^{dim}$
200 neutrophils have been connected with breast cancer lung metastasis[32,33]. As noted in the
201 introduction, CD62L has been implicated in β_2-integrin activation on neutrophils[12], therefore,
202 there may be a mechanistic link between CD62L (either by reduced expression or shedding)
203 and β_2-integrin conformation which results in neutrophil impaired motility in our model. These
204 and the findings above are consistent with the reduction in pro-metastatic neutrophils
205 previously observed upon blocking G-CSF in mammary tumour bearing mice[2].

206

207

208 **Slow moving neutrophils alter blood flow**

209 Finally, we aimed to determine the consequences of neutrophilia and neutrophil speed
210 impairment in lung vasculature. In the context of the work above, we hypothesized that
211 neutrophils could (1) favour the accumulation of circulating tumour cells arriving in lung
212 capillaries as neutrophils have been shown to interact with tumour cells in liver sinusoids and
213 favour their arrest[34,35]; and (2) neutrophils could affect normal blood circulation, as it has been
214 shown that neutrophils can obstruct capillaries in the brain[36,37] and lung[38], impairing blood flow
215 and creating transient circulatory dead spaces.

216 Therefore, we intravenously administered fluorescent beads with a diameter of 10 μm (larger
217 than typical lung capillary size) and 4 μm (slightly smaller than a red blood cell) to control and
218 KP tumour-bearing mice to both 'model' tumour cells and to have a readout of lung blood
219 volume respectively (**Figure 4A**). In addition, mice were treated with either M18/2 or isotype
220 control antibodies to determine whether restoring neutrophil motility affects bead retention in
221 the lung (**Figure 4A**). IHC staining for Ly6G on lung tissue did not indicate a significant
222 difference in neutrophil accumulation in the lungs of tumour-bearing mice treated with isotype
223 control or M18/2 antibody (**Figures 4B and 4C**), in line with what we had observed in the IV-
224 injection model (**Figures 2F and 2I**). 3D fluorescence imaging of fixed PCLS revealed that the
225 retention of 10 μm beads remained unaffected by the presence of primary tumours or antibody
226 treatment, likely due to physical entrapment in the capillaries (**Figures 4D and 4E**). However,
227 significantly fewer 4 μm beads were found in PCLS from tumour-bearing mice treated with
228 isotype control when compared with control mice, supporting the idea of transient formation of
229 circulatory dead spaces in the lung reducing total blood volume (**Figure 4F**). Interestingly,
230 treatment with M18/2 antibody was able to restore a similar bead count to that from control
231 mice, suggesting that restoring neutrophil motility also restores blood circulation (**Figure 4F**).
232 The formation of transient poorly perfused spaces could prevent efficient immune surveillance
233 and protect the tumour cells, supporting a true 'pre-metastatic niche'.

234 Taken together, our results suggest that when primary mammary tumours induce substantial
235 systemic neutrophilia, this aberrant neutrophil population fail to activate the β_2-integrins that
236 would allow normal intravascular motility, causing congestion and impairment of local blood
237 circulation. That this can be recapitulated by treatment of G-CSF to non-tumour bearing mice
238 suggests a role for this potent mediator of neutrophil homeostasis, known to be increased in
239 the tumour microenvironment of mammary tumours[15].

240 In the context of breast cancer metastasis, impaired intravascular neutrophil motility,
241 congestion and reduced local circulatory flux could offer niches inaccessible to anti-tumour

242 immune cells and promote tumour cell seeding indirectly. Additionally, CD11b/CD18 has also
243 been implicated in neutrophil antibody-dependent cellular cytotoxicity (ADCC) of tumour
244 cells[39]. Inactivation of neutrophil integrins could therefore provide another mechanism of
245 immune escape mediated by the primary tumour to favour metastasis at distant sites.

246 Materials & Methods

247 Mice

248 Either female FVB/N mice purchased from Charles River Laboratories (acclimatised for at
249 least 1 week in our mouse facility), or female Catchup$^{IVM\text{-}red}$ mice[13] (identified as *Ly6G*$^{Cre\text{-}tom/+}$
250 *ROSA26*$^{tdtom/+}$, backcrossed onto a FVB/N background for >10 generations and bred in-house)
251 were used for experiments when they were 8-15 weeks old. Age matched mice were randomly
252 allocated to control and transplant/treatment groups. How specific cohorts were analysed is
253 described in the appropriate methods sections and figure legends.

254 Mice were housed (as in [17]) at the CRUK Scotland Institute, UK in specific pathogen-free
255 conditions with a 12 hr light/dark cycle and at a controlled climate of 19-22 °C and 45-65 %
256 humidity. Mice also had access to food and water ad libitum. Mouse procedures were
257 performed in accordance with the UK Animal (Scientific Procedures) Act 1986, approved by
258 the local animal welfare (AWERB) committee, and conducted under UK Home Office licences
259 (PP6345023, P72BA642F and PP0826467) at the CRUK Scotland Institute.

260 Tumour models

261 *Pre-metastatic lung induction.* To induce a pre-metastatic lung, 1 mm^3 mammary tumour
262 fragments obtained from *K14-Cre;Trp53*$^{F/F}$ (KP) mice (maintained on an FVB/N background)[14]
263 were orthotopically transplanted into the 4th mammary fat pad of 10-12 week old female
264 recipient FVB/N or CatchupIVM-red mice using anaesthesia and analgesia. The tumour
265 pieces were allowed to develop into a primary mammary tumour of 10-15 mm in any direction
266 measured three times a week using a calliper and mice were humanely killed usually within a
267 month after transplant. Control mice did not undergo transplantation but were kept in the same
268 conditions.

269 *IV injection models.* For intravenous injection, sub-confluent KP cells, initially obtained from a
270 mammary KP tumour as described before[40], were washed, trypsinized, centrifuged (300 g, 5
271 min), resuspended in medium (RPMI) and passed through a 70 µm cell strainer (Greiner Bio-
272 One). The cells were counted using the CellDrop cell counter (DeNovix), diluted to a maximal
273 concentration of 10^6 cells per mL if necessary and stained with CellTrace (Invitrogen)

274 according to the manufacturer's protocol (Invitrogen). Briefly, cells were incubated with 1 µM
275 CellTrace yellow or far-red in PBS for 20 min at 37 °C. The suspension was then diluted
276 fivefold with culture medium (RPMI) and incubated for 5 min to remove free dye in the solution.
277 Finally, the suspension was centrifuged (300 g, 5 min) and resuspended in PBS before mice
278 were injected intravenously with 100 µL of suspension of $0.5x10^6$ cells and 10 µg of
279 monoclonal antibodies. The following low endotoxin, azide-free purified antibodies were used:
280 isotype control (clone RTK2758, Biolegend), ICAM-1 blocking antibody (clone YN1/1.7.4,
281 Biolegend), CD18-activating antibody (clone M18/2, Biolegend), CD18-blocking antibody
282 (clone GAME-46, BD biosciences).

283 **G-CSF treatment**

284 Female Catchup$^{IVM-red}$ and FVB/N mice aged 8-15 weeks were treated with 5 µg mouse
285 recombinant G-CSF (STEMCELL Technologies) by intraperitoneal injection (i.p.) 24 hours
286 before harvesting the stated tissues.

287 **Flow cytometry**

288 Lungs were excised and then minced with scissors before incubation in RPMI (ThermoFisher)
289 with 10% foetal bovine serum (FBS, ThermoFisher) at 37 °C for 20 min with agitation. Post-
290 incubation, lungs were mashed through a 70 µm filter.

291 Single cell suspensions were stained with Live/Dead stain (LIVE/DEAD Fixable Near-IR,
292 Yellow or Green, Biolegend) and Fc-Receptor block was performed (clone 93, Biolegend).
293 Cell suspensions were incubated with directly conjugated fluorescent antibodies in Brilliant
294 Stain Buffer (BD Horizon) at 4 °C for 30 min.

295 Count beads (CountBright, Life Technologies) were used to determine cell numbers.
296 Compensation was performed using single stained beads (Ultracomp eBeads, ThermoFisher).
297 Acquisition was performed on a BDFortessa using FacsDiva software (BD Biosciences) and
298 data were analysed using FlowJo software (BD).

299 The following antibodies were used:

300 Lung immunophenotyping panel: (all 1:200): CD8-AF488 (clone 53-6.7, Biolegend), CD45-
301 BV711 (clone 30-F11, Biolegend), CD11b-BV650 (clone M1/70 Biolegend), SiglecF-BV605
302 (clone E50-2440 BD Biosciences), F4/80-BV510 (clone BM8, Biolegend), B220-BV421, Ly6G-
303 BUV395 (clone 1A8, BD Biosciences), CD3-AF657 (clone 17A2, Biolegend), CD4-PE/Cy7
304 (clone RM4-5, Biolegend).

305 Neutrophil phenotyping panel: Ter119-FITC (clone TER-119 Biolegend 1:200), NKp46-FITC
306 (clone 29A1.4 Biolegend 1:200), CD115-AF488 (clone AFS98 Biolegend 1:200), CD3-FITC
307 (clone 17A2 Biolegend 1:200), CD19-FITC (clone 6D5 Biolegend 1:200), CD45-BV650 (clone
308 30-F11 Biolegend 1:200), CD11b-BV605 (clone M1/70 Biolegend 1:400), Ly6G-BV510 (clone
309 1A8 Biolegend 1:200), Siglec-F-APC-Cy7 (clone E50-2440 BD Biosciences 1:200), CD18-
310 AF647 (clone M18/2 Biolegend 1:200), CD62L-BUV395 (clone MEL-14 BD Biosciences
311 1:200), CD101-PE-Cyanine7 (clone Moushi101 Invitrogen 1:200).

312 **Fixed PCLS imaging**

313 Precision-cut lung slices (PCLS) were prepared as previously described [41–43]. Mice were
314 humanely killed by overdose of anaesthetic (i.p. injection of sodium-pentobarbital) followed by
315 permanent cessation of the circulation by cutting the femoral artery. A blunted 22G needle
316 was then inserted via a tracheostomy and used to inflate the lungs slowly but continuously
317 with 1 mL of 2% low-melting point agarose (ThermoFisher) prepared in PBS. When flow
318 cytometry of lung tissue was to be performed on the same animals, the left lung was tied off
319 with a suture before lung inflation. Using suture thread, the trachea was then tied to stop
320 agarose leakage before excising lungs, heart and trachea together and placing them in ice-
321 cold PBS. They were then subsequently fixed in 4% formaldehyde (v/v) (FA) in PBS
322 (ThermoFisher) for two hours or overnight. 300 µm lung tissue sections were sliced using a
323 vibrating microtome (5100mz; Campden Instruments) and stainless-steel blades (Model 7550-
324 1-SS; Campden Instruments) with the highest oscillation amplitude, maximal speed, and an
325 advance of 1 mm/sec. Lung sections were stored in PBS/1% (w/v) BSA (Merck)/0.05% (v/v)
326 Sodium Azide (GBiosciences) (PBA) at 4°C. For permeabilization and blocking, samples were
327 incubated in 300 µL permeabilization buffer (PBS, 1% BSA, 0.05% Azide, 10% NGS, 0.3%
328 Triton X 100) for at least one hour. Slices were rinsed with wash buffer (PBS, 1% BSA, 0.05%
329 Azide, 0.1% Triton X 100) before staining with primary antibodies diluted in antibody buffer
330 (PBS, 1% BSA, 0.05% Azide, 10% NGS, 0.1% Triton X 100). Incubation at room temperature
331 in the dark was allowed for at least 3 hours or overnight before washing three times with wash
332 buffer at 37 °C for at least 20 min each. Directly conjugated antibodies, secondary antibodies,
333 and nuclear stains (DAPI or Draq5, 1:1000) diluted in antibody buffer were incubated with the
334 samples for at least 3 h in the dark. If primary and directly conjugated antibodies were derived
335 from the same species (i.e. rat), they were not stained simultaneously. In this case, the slices
336 were washed as above after incubation with the secondary antibody and free antigen binding
337 sites were blocked with appropriate isotype to avoid binding of the secondary antibody to the
338 subsequently used directly conjugated antibodies. Slices were washed twice as above and
339 once with PBS before fixation with 4% FA for 5 mins. FA was removed with two PBS washes

340 before tissue clearing was performed. Clearing with Ce3D including the preparation of the
341 clearing solution has previously been described in detail[19,44]. Briefly, N-methylacetamide was
342 melted and diluted in PBS to prepare a 40% (v/v) stock solution. 86% Histodenz (w/v) was
343 added and allowed to fully dissolve by incubation at 37 °C in a shaking incubator. 0.1% (v/v)
344 Triton X 100 and 0.5% (v/v) 1 thioglycerol were added. Slices were immersed in Ce3D and
345 incubated at room temperature until sufficient clearing was observed. The tissue sections were
346 mounted on microscope slides (VWR) in Ce3D using Frame Seal incubation chambers (Bio
347 Rad) and kept at 4°C in the dark after coverslipping (thickness no. 1.5; VWR). Slices were
348 imaged on a Zeiss LSM 880 confocal microscope using a 32 channel Gallium arsenide
349 phosphide (GaAsP) spectral detector with plan Apo objective lenses (20X/0,8 NA - Air, Carl
350 Zeiss). Samples were excited simultaneously with 405, 488, 561 and 633 laser lines and signal
351 was collected onto the arrayed GaAsp detector in lambda mode with a resolution of 8.9 nm
352 over the visible spectrum. Using reference spectra acquired from either unstained tissue for
353 autofluorescence or single stained tissue for each antibody listed below, the images were then
354 spectrally unmixed using Zen software (Carl Zeiss).

355 The following primary antibodies were used: Hamster anti-mouse CD31 (1:400, clone 2H8,
356 Invitrogen), rat anti-mouse CD8 (1:200, 14-0808-82, ebioscience), S100A9 (1:1000,
357 EPR22332-75, Abcam).

358 The following secondary antibodies were used: Goat Anti-Armenian Hamster polyclonal IgG
359 conjugated with AF488 (1:400, Jackson Immunoresearch), Goat Anti-Rat IgG conjugated with
360 Cy3 (1:400, Jackson Immunoresearch), Goat anti-Rabbit IgG conjugated with AF700 (1:400,
361 Invitrogen). Antibodies with minimal Cross Reactivity to human, bovine, horse, mouse and
362 rabbit serum proteins were preferred.

363 The following conjugated antibodies were used:

364 Anti-mouse I-A/I-E conjugated with BV421 (1:200, clone M5/114.15.2, Biolegend), anti-mouse
365 Podoplanin conjugated with AF488 (1:200, clone PMab-1, Biolegend), anti-mouse CD3
366 conjugated with AF488 (1:200, clone 17A2, Biolegend), anti-mouse CD68 conjugated with
367 AF594 (1:400, clone FA-11, Biolegend)

368 **Cell segmentation and histocytometry analysis**

369 For histocytometry analysis, the method previously published by Li et al.[19] was adapted to the
370 specific needs of the experiment. Gaussian filtering in Imaris was applied on the channels of
371 interest representing specific cell types. Summing was used to generate a merged channel
372 with all stained cell types using the Channel Arithmetic function in Imaris. Multiplier factors

373 served to normalize the channels to one another and obtain similar intensities for all markers
374 in the composite channel. Surface objects were created with the respective module in Imaris.
375 The surface detail in the smooth function was set to 1.4 µm. Background correction was
376 enabled to allow segmentation based on local contrast in areas with differing background
377 intensities such as bronchi with high autofluorescence. A threshold was set to incorporate all
378 cell derived signals while excluding unspecific background. The split touching objects option
379 was enabled and set to 8 µm, i.e. the approximate mean size of the observed cell types. Seed
380 points were filtered to only include events with sufficient signal intensity. After verifying an
381 adequate representation of the cells of interest by the created surface objects, the statistics
382 for these objects were exported into CSV files.

383 Relevant parameters were combined into one Excel file applying the RDBMerge plugin
384 (http://www.rondebruin.nl/win/addins/rdbmerge.htm) for automation of the process. In our
385 experiments, mean and summed channel intensity, volume, area, and position are the crucial
386 parameters. These data were saved in a CSV file which can subsequently be opened in
387 FlowJo for phenotypic gating and quantification of different cell populations like typical flow
388 cytometry analysis.

389 Interactions between stained $CD8^+$ T cells and $Ly6G^+$ Neutrophils were quantified based on
390 the distance between one cell and the nearest cell of the other cell type. To achieve this, spots
391 and surface objects were generated in Imaris for both cell types respectively and the 'Find
392 spots close to surface' XTension was used to define the subset of cells that interact with the
393 other cell type, i.e. spots that are within the set threshold distance of 8 µm from a surface
394 object.

395 **Live PCLS imaging**

396 All mice used for neutrophil dynamics analysis were humanely killed within the same period
397 (between 09.00-10.30) to minimize circadian-induced changes between samples. Where
398 cohorts needed to be split over several imaging sessions, each imaging session was carried
399 out with at least one age-matched control. Live PCLS procedure was performed as in [41]. Lungs
400 were inflated with low melting agarose point as above. Excised lungs were placed in ice-cold
401 PBS. Lungs were sliced into 300µm thick sections on a vibratome and stained with directly
402 conjugated antibodies, Hoechst and probes for reactive superoxide and nitric oxide (ROS-ID®
403 ROS/RNS detection kit, Enzo Life Sciences) in complete medium (phenol-red free DMEM
404 substituted with 10% FBS) for 20 minutes at 37°C. For *ex vivo* integrins activation experiments,
405 isotype control (clone RTK2758, Biolegend) or CD18-activating (clone M18/2, Biolegend)
406 antibodies were added to the solution at 1:50 dilution.

407 The following antibodies were used (all 1:200): Anti-mouse CD31-BV421 (clone 390,
408 Biolegend), anti-mouse CD8-AF488 (clone 53-6.7, Biolegend), anti-mouse Ly6G-DyLight550
409 (clone 1A8, Novus Biologicals), anti-mouse CD11c-AF594 (clone N418, Biolegend), anti-
410 mouse CD45 Spark NIR685 (clone 30-F11, Biolegend).
411
412 Slices were imaged on a Zeiss LSM880 confocal microscope using multiwell incubation
413 chambers (Ibidi µ-Slide 8-well or Nunc Lab-Tek II 8-well Chamber Slide System) at 37°C with
414 5% CO2. Lung slices were imaged for 6 to 40min with z-stacks of 22-35µm. Acquisition was
415 performed with a 32 channel Gallium arsenide phosphide (GaAsP) spectral detector plan Apo
416 objective lenses (20X/0,8 NA - Air, Carl Zeiss). Samples were excited simultaneously with
417 405, 488, 561 and 633 laser lines and signal was collected onto a linear array of the 32 GaAsp
418 detectors in lambda mode with a resolution of 8.9 nm over the visible spectrum. Spectral
419 images were then unmixed with Zen software (Carl Zeiss) using reference spectra acquired
420 from unstained tissues (tissue autofluorescence) or slides containing single fluorophores.

421 **4D image analysis**

422 Timelapse image analysis and visualization was performed using Imaris (Bitplane).
423 Neutrophils and $CD8^+$ T cells were segmented and tracked using the 'surface' tool using either
424 Ly6G fluorescence intensity (neutrophils) or CD8 (T-cells). All surfaces and tracks were
425 checked manually to avoid any false detections. Oxidative stress was measured with
426 superoxide/nitric oxide mean cell fluorescence and cell behaviour was determined using the
427 mean track speed.

428 **Immunohistochemistry (IHC)**

429 Lungs were fixed in 4% buffered formalin overnight. Fixative was changed 24 h post-fixation
430 for a further 24 h. Thereafter, lungs were dehydrated in increasing concentrations of 70% to
431 100% ethanol, and then placed in xylene before paraffin embedding. Four-micron-thick serial
432 sections were prepared as previously published[43]. Immunostaining for neutrophils was
433 performed at the CRUK Scotland Institute's Histology Facility. Antigen retrieval was performed
434 using ER2 retrieval buffer (20 min, 95 °C). Sections were then stained for Ly6G (clone 1A8)
435 at a previously optimized dilution (1:60000) for 30 min at room temperature with the
436 autostainer Bond Rx (Leica Microsystems GmbH, Wetzlar, Germany). The IHC sections were
437 visualised with 3,3'Diaminobenzidine (DAB). Stained sections were then digitally scanned
438 using a Leica Aperio AT2 slide scanner at ×20 magnification. Digital slides were analysed with
439 QuPath[45]. Lung sections were annotated using 'pixel classification' and DAB positive cells

440 within the annotated areas were detected using the “positive cell detection” tool. Results were
441 then expressed as the number of positive cells/mm^2 of lung tissue.

442 **Fluorescent beads retention in the lung**

443 Once outgrown tumours reached 12mm in any direction, mice were injected intraperitoneally
444 with 20µg of CD18 activating antibody (clone M18/2, Biolegend) or Isotype control (clone
445 RTK2758, Biolegend) in 100µL PBS. 24h later, mice were injected intravenously with a 100µL
446 mixture containing 10µg of CD18 activating antibody or isotype control, 500 000 blue-
447 fluorescent Polystyrene Microspheres, diameter 10 µm (FluoSpheres, Thermofisher) and
448 20uL of a solution (2% solids) of yellow/green-fluorescent Sulfate Microspheres, diameter 4.0
449 µm (FluoSpheres, Thermofisher). Mice were culled for lung collection 15 minutes after
450 injection and lung were processed for fixed PCLS imaging (see above). Cleared PCLS were
451 imaged using an Opera Phenix (Perkin Elmer) high throughput spinning disk microscope.
452 Images were analysed using Imaris (Bitplane) to measure the number of beads / mm^3 in the
453 lung sections.

454 **Statistics**

455 Representation and data analysis were performed with Prism 9.0 and 10.0 software
456 (GraphPad Inc.). The choice of statistical analysis was based on sample size and distribution
457 of samples. Normality was assessed via the Shapiro–Wilk test. Data from independent
458 experiments were pooled when possible. Where normality could be determined (1) parametric
459 t-tests were used to compare two groups; (2) One-way analysis of variance (ANOVA) was
460 used to compare three groups according to one variable (antibody treatment); (3) Two-way
461 ANOVA, followed with Sídák’s multiple comparisons tests was performed to analyse the
462 influence of two independent variables (tumour presence and/or antibody treatment). When
463 normality could not be determined, or data were not normally distributed, multiple Mann-
464 Whitney test was performed with multiple comparisons correction using the Holmes- Sídák to
465 compare multiple groups. Specific tests used in each case are stated in the figure legends.
466 Means +/- standard error of the mean are indicated were possible. Specific numbers of
467 animals can be found in corresponding figure legends.

468 ## References

469 1. McFarlane, A. J., Fercoq, F., Coffelt, S. B. & Carlin, L. M. Neutrophil dynamics in the
470 tumor microenvironment. *J. Clin. Invest.* **131**, (2021).
471 2. Coffelt, S. B. *et al.* IL-17-producing γδ T cells and neutrophils conspire to promote breast
472 cancer metastasis. *Nature* **522**, 345–348 (2015).
473 3. Wculek, S. K. & Malanchi, I. Neutrophils support lung colonization of metastasis-initiating
474 breast cancer cells. *Nature* **528**, 413–417 (2015).
475 4. Gong, Z. *et al.* Immunosuppressive reprogramming of neutrophils by lung mesenchymal
476 cells promotes breast cancer metastasis. *Sci. Immunol.* **8**, (2023).
477 5. Maru, Y. The lung metastatic niche. *J. Mol. Med.* **93**, 1185–1192 (2015).
478 6. Quail, D. F. *et al.* Neutrophil phenotypes and functions in cancer: A consensus statement.
479 *J. Exp. Med.* **219**, (2022).
480 7. Xiao, W. *et al.* Risk factors and survival outcomes in patients with breast cancer and lung
481 metastasis: a population-based study. *Cancer Med.* **7**, 922–930 (2018).
482 8. Chen, M.-T. *et al.* Comparison of patterns and prognosis among distant metastatic breast
483 cancer patients by age groups: a SEER population-based analysis. *Sci. Rep.* **7**, 9254
484 (2017).
485 9. Cardoso, F. *et al.* Global analysis of advanced/metastatic breast cancer: Decade report
486 (2005–2015). *The Breast* **39**, 131–138 (2018).
487 10. Snelgrove, R. J., Godlee, A. & Hussell, T. Airway immune homeostasis and
488 implications for influenza-induced inflammation. *Trends Immunol.* **32**, 328–334 (2011).
489 11. Bouti, P. *et al.* β2 Integrin Signaling Cascade in Neutrophils: More Than a Single
490 Function. *Front. Immunol.* **11**, (2021).
491 12. Stadtmann, A. *et al.* The PSGL-1–L-selectin signaling complex regulates neutrophil
492 adhesion under flow. *J. Exp. Med.* **210**, 2171–2180 (2013).
493 13. Hasenberg, A. *et al.* Catchup: a mouse model for imaging-based tracking and
494 modulation of neutrophil granulocytes. *Nat. Methods* **12**, 445–452 (2015).

495 14. Liu, X. *et al.* Somatic loss of BRCA1 and p53 in mice induces mammary tumors with
496 features of human BRCA1-mutated basal-like breast cancer. *Proc. Natl. Acad. Sci.* **104**,
497 12111–12116 (2007).
498 15. Wellenstein, M. D. *et al.* Loss of p53 triggers WNT-dependent systemic inflammation
499 to drive breast cancer metastasis. *Nature* **572**, 538–542 (2019).
500 16. Li, P. *et al.* Lung mesenchymal cells elicit lipid storage in neutrophils that fuel breast
501 cancer lung metastasis. *Nat. Immunol.* **21**, 1444–1455 (2020).
502 17. John B. G. Mackey *et al.* Maturation, developmental site, and pathology dictate
503 murine neutrophil function. *bioRxiv* (2021).
504 18. Gerner, M. Y., Kastenmuller, W., Ifrim, I., Kabat, J. & Germain, R. N. Histo-
505 Cytometry: A Method for Highly Multiplex Quantitative Tissue Imaging Analysis Applied to
506 Dendritic Cell Subset Microanatomy in Lymph Nodes. *Immunity* **37**, 364–376 (2012).
507 19. Li, W., Germain, R. N. & Gerner, M. Y. High-dimensional cell-level analysis of tissues
508 with Ce3D multiplex volume imaging. *Nat. Protoc.* **14**, 1708–1733 (2019).
509 20. Ballesteros, I. *et al.* Co-option of Neutrophil Fates by Tissue Environments. *Cell* **183**,
510 1282-1297.e18 (2020).
511 21. Bae, G. H. *et al.* Unique characteristics of lung-resident neutrophils are maintained
512 by PGE2/PKA/Tgm2-mediated signaling. *Blood* **140**, 889–899 (2022).
513 22. De Donatis, M., Fercoq, F. & Carlin, L. M. Imaging Inflammation by Intravital
514 Microscopy. in *Imaging Inflammation* (eds. Man, F. & Cleary, S. J.) 223–241 (Springer
515 International Publishing, Cham, 2023).
516 23. Devi, S. *et al.* Multiphoton imaging reveals a new leukocyte recruitment paradigm in
517 the glomerulus. *Nat. Med.* **19**, 107–112 (2013).
518 24. Auffray, C. *et al.* Monitoring of Blood Vessels and Tissues by a Population of
519 Monocytes with Patrolling Behavior. *Science* **317**, 666–670 (2007).
520 25. Conrad, C. *et al.* ADAM8 signaling drives neutrophil migration and ARDS severity.
521 *JCI Insight* **7**, (2022).

522 26. Lämmermann, T. *et al.* Rapid leukocyte migration by integrin-independent flowing
523 and squeezing. *Nature* **453**, 51–55 (2008).
524 27. Petrovich, E. *et al.* Lung ICAM-1 and ICAM-2 support spontaneous intravascular
525 effector lymphocyte entrapment but are not required for neutrophil entrapment or
526 emigration inside endotoxin-inflamed lungs. *FASEB J.* **30**, 1767–1778 (2016).
527 28. Yipp, B. G. *et al.* The lung is a host defense niche for immediate neutrophil-mediated
528 vascular protection. *Sci. Immunol.* **2**, eaam8929 (2017).
529 29. Varga, G. *et al.* Active MAC-1 (CD11b/CD18) on DCs inhibits full T-cell activation.
530 *Blood* **109**, 661–669 (2006).
531 30. Headley, M. B. *et al.* Visualization of immediate immune responses to pioneer
532 metastatic cells in the lung. *Nature* **531**, 513–517 (2016).
533 31. Evrard, M. *et al.* Developmental Analysis of Bone Marrow Neutrophils Reveals
534 Populations Specialized in Expansion, Trafficking, and Effector Functions. *Immunity* **48**,
535 364-379.e8 (2018).
536 32. Wang, Z. *et al.* CD62Ldim Neutrophils Specifically Migrate to the Lung and
537 Participate in the Formation of the Pre-Metastatic Niche of Breast Cancer. *Front. Oncol.*
538 **10**, (2020).
539 33. Wang, Z. *et al.* Tumor-derived HMGB1 induces CD62Ldim neutrophil polarization
540 and promotes lung metastasis in triple-negative breast cancer. *Oncogenesis* **9**, 82 (2020).
541 34. McDonald, B. *et al.* Systemic inflammation increases cancer cell adhesion to hepatic
542 sinusoids by neutrophil mediated mechanisms. *Int. J. Cancer* **125**, 1298–1305 (2009).
543 35. Spicer, J. D. *et al.* Neutrophils Promote Liver Metastasis via Mac-1–Mediated
544 Interactions with Circulating Tumor Cells. *Cancer Res.* **72**, 3919–3927 (2012).
545 36. El Amki, M. *et al.* Neutrophils Obstructing Brain Capillaries Are a Major Cause of No-
546 Reflow in Ischemic Stroke. *Cell Rep.* **33**, 108260 (2020).
547 37. Cruz Hernández, J. C. *et al.* Neutrophil adhesion in brain capillaries reduces cortical
548 blood flow and impairs memory function in Alzheimer's disease mouse models. *Nat.*
549 *Neurosci.* **22**, 413–420 (2019).

550 38. Inwon Park *et al.* Neutrophils disturb pulmonary microcirculation in sepsis-induced
551 acute lung injury. *Eur. Respir. J.* **53**, 1800786 (2019).
552 39. Matlung, H. L. *et al.* Neutrophils Kill Antibody-Opsonized Cancer Cells by
553 Trogoptosis. *Cell Rep.* **23**, 3946-3959.e6 (2018).
554 40. Millar, R. *et al.* The MSP-RON axis stimulates cancer cell growth in models of triple
555 negative breast cancer. *Mol. Oncol.* **14**, 1868–1880 (2020).
556 41. McCowan, J. *et al.* The transcription factor EGR2 is indispensable for tissue-specific
557 imprinting of alveolar macrophages in health and tissue repair. *Sci. Immunol.* **6**, (2021).
558 42. Fercoq, F. *et al.* IL-4 receptor dependent expansion of lung CD169+ macrophages in
559 microfilaria-driven inflammation. *PLoS Negl. Trop. Dis.* **13**, (2019).
560 43. Fercoq, F. *et al.* Microfilaria-dependent thoracic pathology associated with
561 eosinophilic and fibrotic polyps in filaria-infected rodents. *Parasit. Vectors* **13**, (2020).
562 44. Li, W., Germain, R. N. & Gerner, M. Y. Multiplex, quantitative cellular analysis in
563 large tissue volumes with clearing-enhanced 3D microscopy (Ce3D). *Proc. Natl. Acad.*
564 *Sci.* **114**, E7321–E7330 (2017).
565 45. Bankhead, P. *et al.* QuPath: Open source software for digital pathology image
566 analysis. *Sci. Rep.* **7**, 16878 (2017).

567

Acknowledgments

We are grateful to Catherine Winchester (CRUK Scotland Institute) for critical reading and checking of the manuscript. We are grateful for support from all the services and resources at the CRUK Scotland Institute with particular thanks to the Biological Services Unit, the Beatson Advanced Imaging Resource (BAIR), the Flow Cytometry Facility and the Histology Facility. We also thank the MNHN light microscopy facility (CeMIM, Centre de Microscopie et d'IMagerie numérique, MNHN Paris) for providing access to Confocal scanning laser microscopes. We thank Jos Jonkers (Netherlands Cancer Institute) for the KP mammary cancer mouse model. Illustrations were created with BioRender.com.

Data availability

Upon acceptance, all data will be made available by the corresponding author on request.

Competing interests

LMC has consulted for Ono Pharmaceuticals UK, JBGM has subsequently become an employee of AstraZeneca, AJM has subsequently become an employee of Antibody Analytics

Funding

FF, GSC, SBC & LMC were supported by Breast Cancer Now grant 2019DecPR1424 and CRUK Scotland Centre core - CTRQQR-2021\100006
LMC, FF, GSC, MDD, JBGM, XLRI, AM, LWGA were supported by CRUK SI core programme to LMC A23983 and CRUK SI core funding to the CRUK Scotland Institute A31287
LMC - DRCRPG-Nov22/100007
JCN, DW - CRUK Core A28291
CN - CRUK SI core A31287
LB – Wellcome Trust Biomedical Vacation Scholarship 220281/Z/20/Z
EWR - CRUK SI core A1920
KB - CRUK SI Core A29799 CRUK SI core A31287

Author contributions

Conceptualization – FF, GSC, SBC, LMC
Formal analysis – FF, GSC
Funding acquisition- JCN, EWR, KB, SBC, LMC
Investigation – FF, GSC, MDD, JBGM, AF, AM, XLR, DW, LWGA, CN, RW, AK, LB, SA-K
Methodology – FF, KB, SC
Project administration – LMC
Resources – RW, AK, SBC
Supervision – JCN, EWR, KB, SBC, LMC

Validation – FF, GSC, DW
Visualization – FF, GSC
Writing – original draft – FF, GSC, LMC.

607 **Figures**

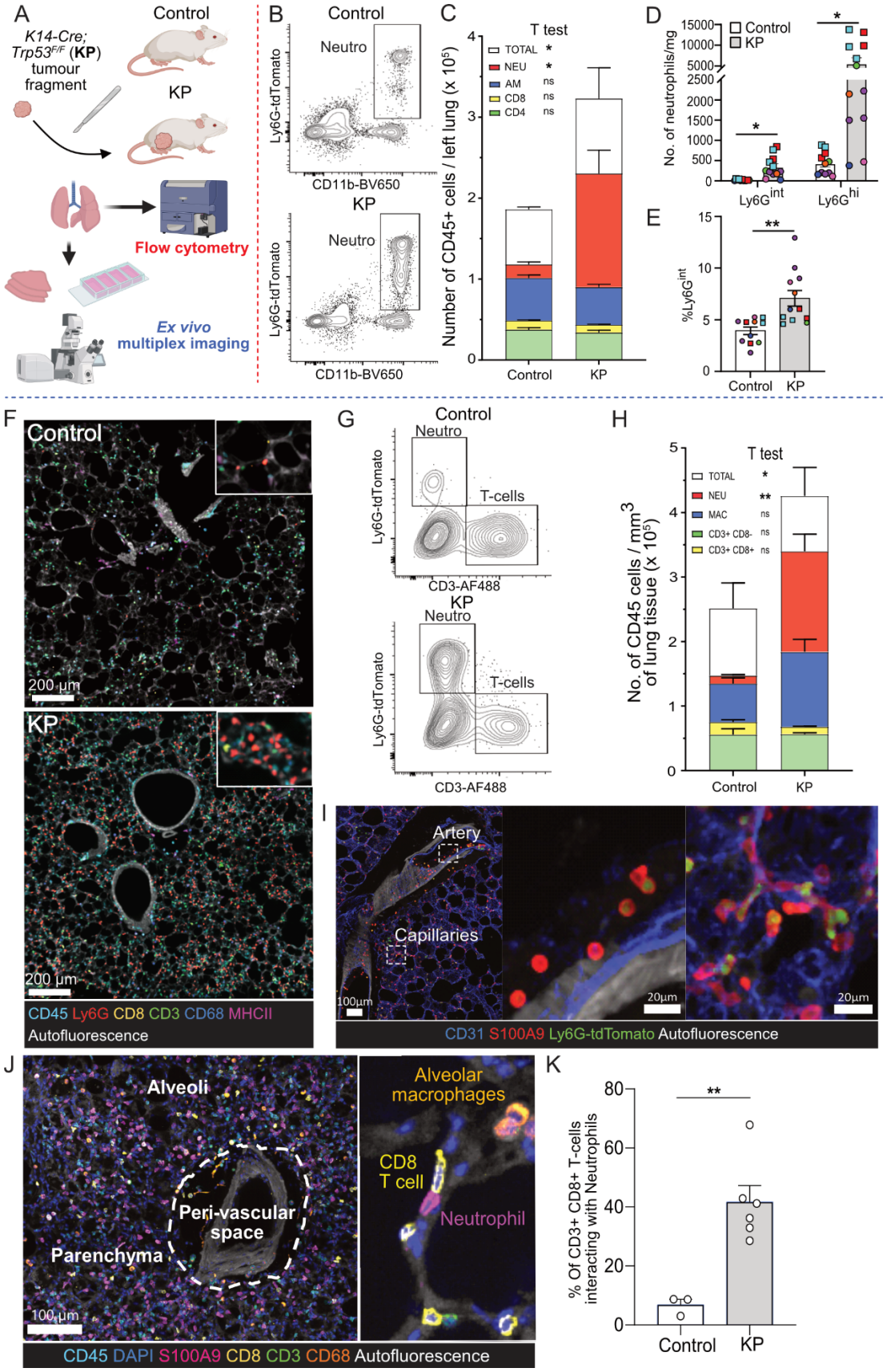

608

609 **Figure 1: The pre-metastatic lung is congested with neutrophils.**

610 (A) Schematic of tumour transplant model and experimental setup.
611 (B-C) Flow cytometry analysis of lungs (using lung immunophenotyping panel) from age-matched non-
612 transplanted control and orthotopic KP 10-15 mm tumour-bearing Catchup$^{IVM-red}$ Ly6G reporter mice.
613 (B) Representative gated plots of CD11b^{+} Ly6G$^{tdtomato+}$ neutrophils, see **Figure S2A** for full gating
614 strategy. (C) Quantification of the different CD45^{+} cell populations. NEU: neutrophils; AM: alveolar
615 Macrophages; CD8: CD8+ T-lymphocytes, CD4: CD4+ T-Lymphocytes. Results are expressed as
616 mean ± SEM of n = 3 control and 6 tumour-bearing Catchup$^{IVM-red}$ mice. Unpaired T-tests were
617 performed for each cell type, *p≤0.05.
618 (D-E) Flow cytometry analysis of Ly6G expression (using neutrophil phenotyping panel) in the lungs.
619 Results are expressed as mean ± SEM of n = 11 control and 12 10-15 mm tumour-bearing mice. Two
620 independent transplant cohorts; squares – cohort one Catchup$^{IVM-red}$ mice, circles – cohort two WT mice.
621 Each colour represents mice which were harvested on the same day when tumours reached endpoint.
622 See **Figure S2B** for gating strategy. (D) Quantification of number of Ly6G^{int} and Ly6G^{hi} neutrophils per
623 mg of lung tissue. A multiple Mann-Whitney test with Holm-Šídák multiple comparisons correction,
624 *p≤0.05. (E) % Ly6G^{int} neutrophils. Unpaired parametric t-test, **p≤0.01.
625 (F-I) Chemically cleared precision-cut lung slices (PCLS) imaged by spectral multiplexed
626 immunofluorescence confocal microscopy as in **Figure S2C**. (F) Maximum intensity projections of
627 spectrally unmixed PCLS images stained with CD3-AF488, CD8-Cy3, CD68-AF594, MHCII-BV421 and
628 a mix of CD45+CD19+CD11c-AF647 in addition to the tdTomato reporter for Ly6G. Autofluorescence
629 was also unmixed and provided tissue architecture information. (G) Leukocytes were segmented, and
630 cell fluorescence intensity was imported in a flow-cytometry analysis software. Figure shows
631 representative plots. (H) Quantification of the different cell populations by histocytometry of
632 fluorescence images. Results, mean ± SEM of n = 3 control and 6 tumour-bearing mice Catchup$^{IVM-red}$
633 mice. Unpaired T-tests for each cell type, *p≤0.05, **p≤0.01.
634 (I) Fixed PCLS were imaged for neutrophils (S100A9 and Ly6G^{tdTomato}) along with CD31 (blue) staining
635 of vascular endothelium. Dashed squares indicate zoomed on an artery area showing round neutrophils
636 or constricted neutrophils in capillaries.
637 (J) Maximum intensity projection of a spectrally unmixed multiplexed confocal microscopy image of a
638 PCLS from a KP tumour bearing FVB/N mouse stained with CD45-Dylight685, DAPI, S100A9-AF700,
639 CD8-Cy3, CD3-AF488 and CD68-AF594. Autofluorescence was also unmixed and provided tissue
640 architecture information. The close-up view of the lung parenchyma shows neutrophil-CD8^{+} T cell
641 interaction in lung capillaries.
642 (K) Quantification of neutrophil-T-cell interactions in PCLS from control and KP-tumour Catchup$^{IVM-red}$
643 bearing mice. Results as mean ± SEM of n = 3 control and 6 tumour-bearing mice (related to images in
644 figure 1E-G), T-test **p≤0.01. Flow cytometry (B-C) and (D-E) and imaging results (F-I) were obtained
645 from four independent experiments.

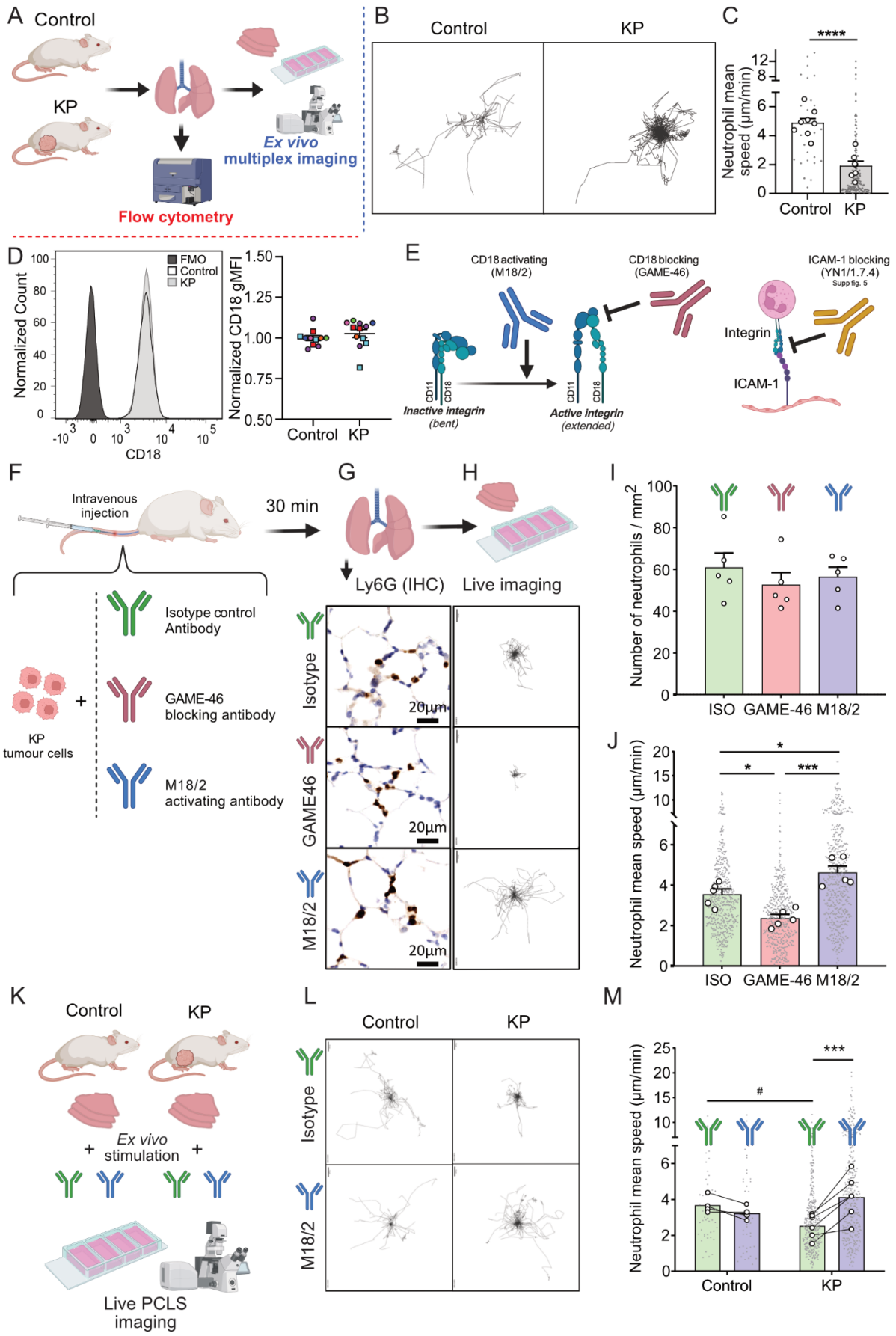

646

647 **Figure 2: Neutrophils in the pre-metastatic are slow-moving due to integrin inactivation.**

648 (A) Schematic of the experiment design. Lungs from age-matched non-transplanted control and 10-15
649 mm orthotopic KP tumour-bearing FVB/N mice were harvested for live precision-cut lung slices (PCLS)
650 imaging or flow cytometry.
651 (B-C) Neutrophil tracking in live multiplexed confocal microscopy timelapse images of *ex vivo* PCLS
652 from control and KP tumour-bearing mice (see video S1). (B) Representative neutrophil tracking centred
653 plots (spider plot). (C) Quantification of neutrophil mean speed. Grey dots represent the speed of each
654 individual neutrophil (24-148 tracks per group were analysed) while white dots represent the mean
655 speed in each mouse. The mean value per animal were used to perform an unpaired parametric T-test,
656 ****$p \leq 0.0001$. Results are expressed as mean ± SEM of n= 8 control and 6 tumour-bearing FVB/N mice.
657 (D) Flow cytometry of CD18 expression on lung neutrophils (using neutrophil phenotyping panel). Left:
658 representative histogram. Fluorescence minus one (FMO) for CD18 also shown. Right: quantification
659 of CD18 geometric mean fluorescence intensity (gMFI). Results are expressed as mean ± SEM of n =
660 11 control and 12 tumour-bearing mice. Two independent transplant cohorts; squares – cohort one
661 Catchup$^{IVM-red}$ mice, circles – cohort two WT mice. Results normalized to the mean of controls harvested
662 the same day (same coloured points). **Figure S2B** for gating strategy. nonparametric Mann-Whitney
663 test, ns>0.05.
664 (E) Schematic of integrin conformational changes controlling integrin activation and integrin binding to
665 ICAM-1. The M18/2 antibody stabilizes the active conformation, whereas the GAME-46 antibody blocks
666 the CD18 active domain. YN1/1.7.4 antibody blocks ICAM-1 (see **Figure S6**).
667 (F-J) Modulation of neutrophil motility in an intravenous (IV) transplant model of KP cells, using CD18
668 activating and blocking antibodies. (F) Schematic of the experiment design. Mice were IV injected with
669 KP cells and either isotype control antibody (green), GAME-46 (pink), or M18/2 (blue). 30 minutes later
670 lungs were taken for live *ex vivo* confocal microscopy of PCLS (see **video S2**) and
671 Immunohistochemistry (IHC). (G) Representative IHC from the three treatment groups. (H)
672 Representative neutrophil tracking plots from the three treatment groups. (I) Quantification of the
673 number of neutrophils/mm^2 in lung IHC. Results expressed as mean ± SEM of 5 mice per group. One-
674 way ANOVA. (J) Quantification of neutrophil speed in live *ex vivo* microscopy. Grey dots represent the
675 speed of individual neutrophils (a total of 482-913 tracks per group were analysed; display was cropped
676 at 512 tracks) while white dots represent the mean neutrophil speed/mouse. Mean value per mouse in
677 ANOVA. (G-J) Results, mean ± SEM of n = 5 mice per group, pool of 5 independent experiments with
678 1 mouse per group. *$p \leq 0.05$, ***$p \leq 0.001$.
679 (K-M) *Ex vivo* stimulation of live PCLS from control and KP tumour-bearing mice. (K) Schematic. Live
680 lungs from age-matched controls and 10-15 mm KP-tumour bearing mice, live PCLS stimulated with
681 either isotype control antibody or M18/2 in a chamber slide. (L) Representative neutrophil tracking plots.
682 (M) Quantification of neutrophil mean speed. Grey dots represent the speed of individual neutrophils (a
683 total of 44-371 tracks per group were analysed) while white dots represent the mean neutrophil speed
684 per mouse. Results are expressed as mean ± SEM of n =4 control mice and 6 KP-tumour bearing
685 Catchup$^{IVM-red}$ mice. A Two-way Repeated Measure ANOVA followed with Sídák's multiple
686 comparisons tests was performed. *** $p \leq 0.001$ for differences between isotype and M18/2 antibodies,
687 $^{\#}p \leq 0.05$ for differences between control and KP tumour bearing mice.

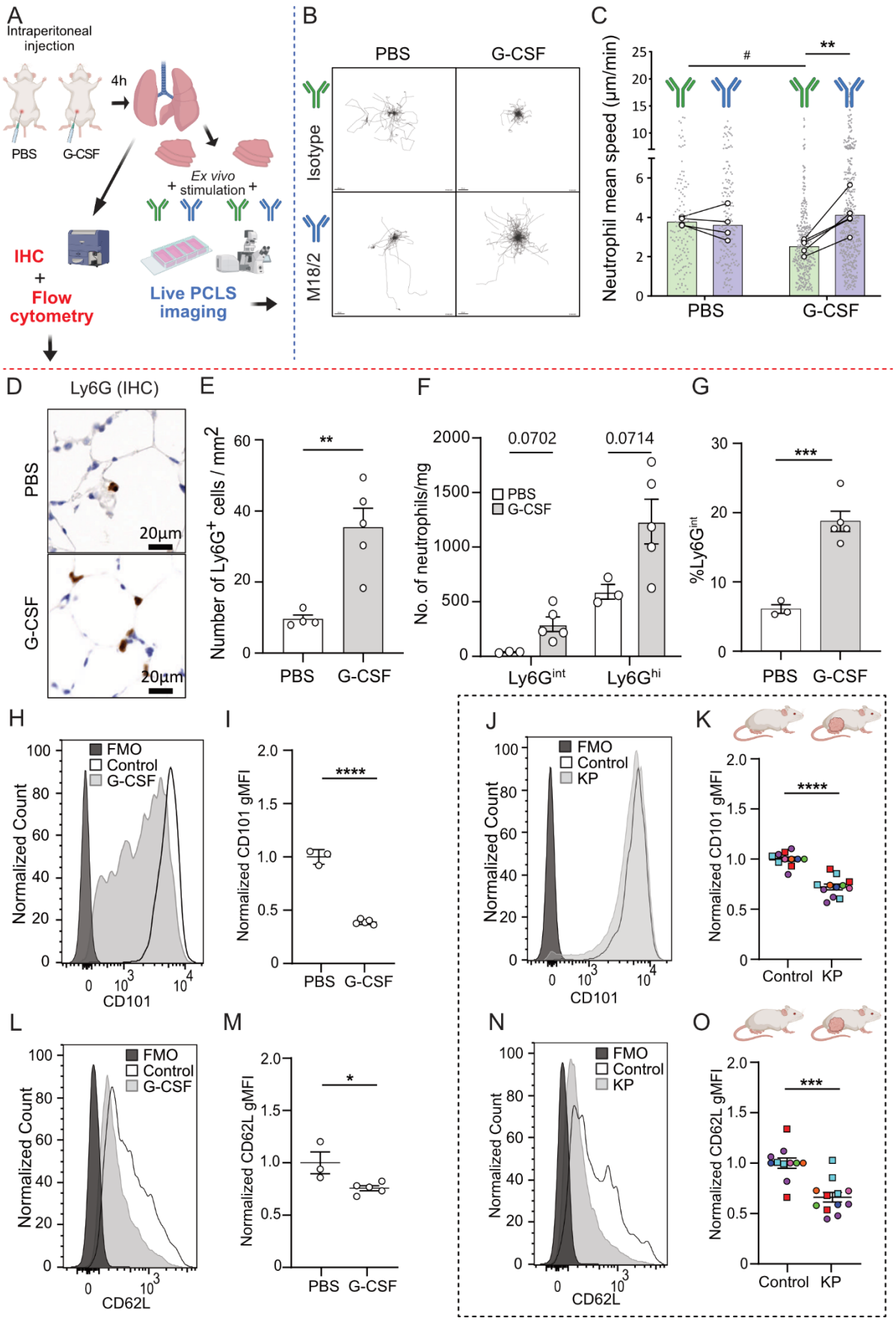

688

689 **Figure 3: G-CSF induces mobility inhibition by impairing CD18 activation.**

690 (A) Schematic of experiment design. Mice were IP injected with either PBS or 5 µg G-CSF. 24 hours
691 later lungs were taken for IHC, flow cytometry and/or live *ex vivo* multiplexed confocal microscopy of
692 PCLS stimulated with either isotype control or M18/2.
693 (B) Representative neutrophil tracking plots of live PCLS from PBS and G-CSF treated FVB/N mice,
694 stimulated *ex vivo* with either isotype antibodies or M18/2.
695 (C) Quantification of mean neutrophil speed from live multiplexed confocal microscopy. Grey dots
696 represent the speed of individual neutrophils (a total of 128-482 tracks per group were analysed) while
697 white dots represent the mean speed per mouse. A Two-way Repeated Measure ANOVA followed with
698 Sídák's multiple comparisons test was performed on the mean values. Results are expressed as mean
699 ± SEM of n = 4 PBS control and 5 G-CSF treated FVB/N mice, ** $p \leq 0.01$ for differences between isotype
700 and M18/2 antibodies, $^{\#}p \leq 0.05$ for differences between control and G-CSF treated mice.
701 (D) Representative Ly6G IHC images from PBS and G-CSF treated FVB/N mice.
702 (E) Quantification of number of $Ly6G^{+}$ cells (neutrophils)/mm^2 of lung tissue in IHC images. Results are
703 expressed as mean ± SEM of n = 4 PBS control and 5 G-CSF treated mice. An unpaired parametric T-
704 test was performed. **$p \leq 0.01$.
705 (F-O) Flow cytometry of lung neutrophils (using neutrophil phenotyping panel), see **Figure S2B** for
706 gating strategy. (F-I, L-M) Mean ± SEM of n = 3 PBS control and 5 G-CSF treated $Catchup^{IVM\text{-}red}$ mice.
707 (J-K, N-O) Comparable flow cytometry of lung neutrophils in KP transplant mice (black dashed box).
708 Mean ± SEM of n = 11 control and 12 tumour-bearing mice. Two independent transplant cohorts;
709 squares – cohort one are $Catchup^{IVM\text{-}red}$ mice, circles – cohort two are FVB/N WT mice.
710 (F) No. $Ly6G^{int}$ immature and $Ly6G^{hi}$ mature neutrophils/mg lung tissue. Mann-Whitney with Holm-Šídák
711 multiple comparisons correction. (G) % of $Ly6G^{int}$ neutrophils. T-test ***$p \leq 0.001$. (H) Representative
712 CD101 histogram. (I) CD101 gMFI normalized to mean of controls. T-test ****$p \leq 0.0001$.
713 (J) Representative CD101 histogram. (K) CD101 gMFI normalized to the mean of the controls harvested
714 on the same day (same coloured points). T-test ****$p \leq 0.0001$.
715 (L) Representative CD62L histogram. (M) CD62L gMFI normalized to mean of controls. T-test *$p \leq 0.05$.
716 (N) Representative CD62L histogram. (O) CD62L gMFI normalized to the mean of the controls
717 harvested on the same day (same coloured points). T-test, ***$p \leq 0.001$.

718

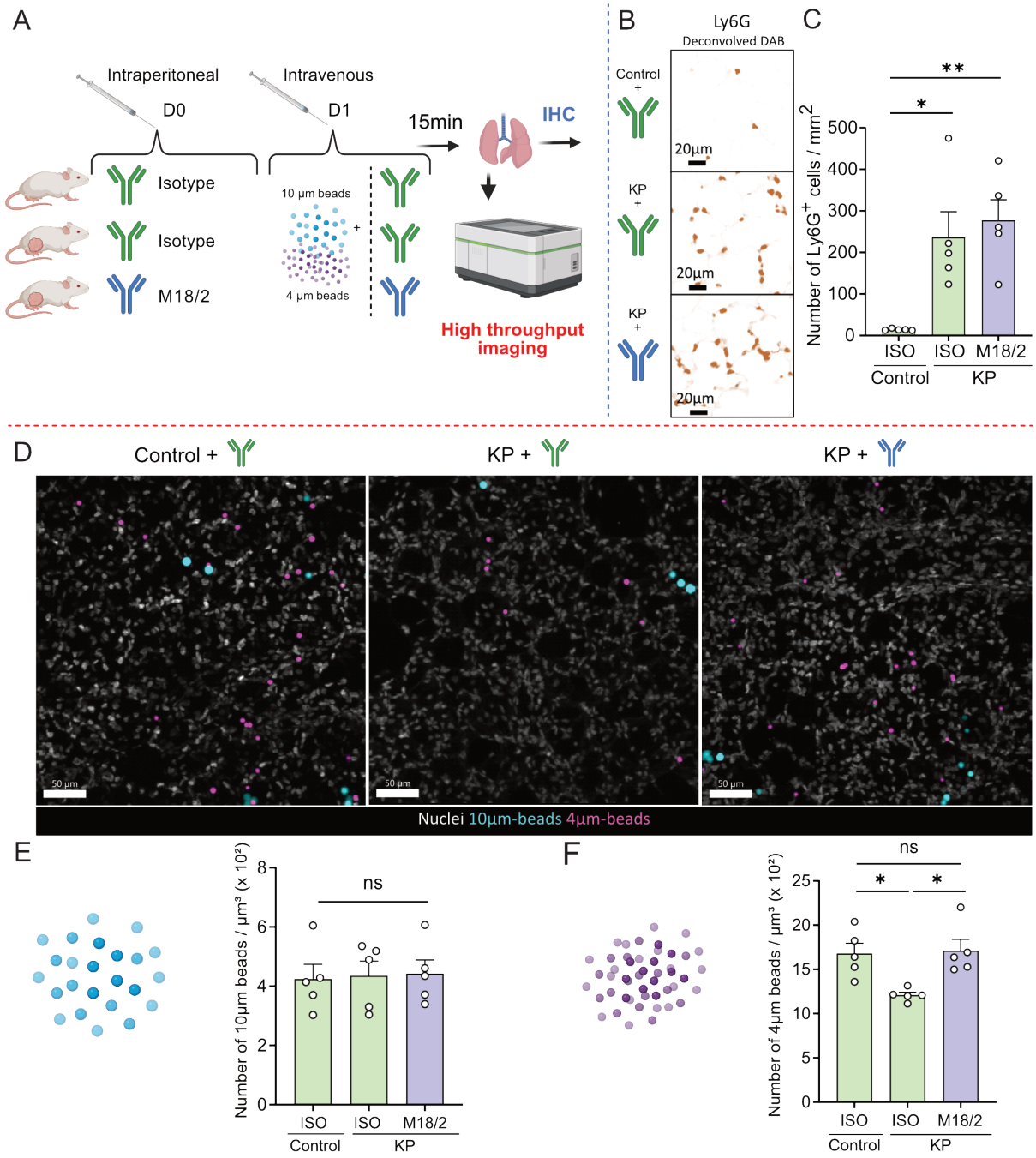

Figure 4. Slowed neutrophils in the pre-metastatic lung restricts blood flow.

(A) Schematic of experiment design. 4- and 10-µm fluorescent beads were intravenously injected to control and KP tumour-bearing FVB/N mice along with either M18/2 or isotype control antibodies. Lungs were there harvested for (B-C) Ly6G IHC quantification and (D-F) high throughput confocal fluorescence imaging of fixed PCLS.

(B) Representative IHC images from the three different experiment groups. (C) Quantification of the number of Ly6G$^+$ cells per mm^2 of lung tissue. Results are expressed as mean ± SEM of n = 5 mice per group. A one-way ANOVA with Šídák's multiple comparison test was carried out (*p≤0.05, and **p≤0.01).

(D-F) High throughput confocal fluorescence imaging of fixed PCLS to quantify number of beads in the slices. (D) Representative individual field of views for the three experiment groups where DNA was labelled with DRAQ5. (E) Quantification of the number of 10µm beads per μm^3. (F) Quantification of the number of 4µm beads per μm^3. Results are expressed as mean ± SEM of n = 5 mice per group (same mice as in B-C). A one-way ANOVA with Šídák's multiple comparison tests was carried out (*$p \leq 0.05$).

735 **Supplementary figures and legends**

736 **Video 1: Neutrophil behaviour and free radical production in live PCLS.**

737 Lungs from 10-15 mm KP tumour bearing mice were harvested for live *ex vivo* multiplexed confocal
738 microscopy of PCLS to analyse their behaviour and free radical production (Reactive Oxygen Species
739 – ROS and Reactive Nitrogen Species – RNS). Slices were stained for DNA (Hoechst, blue),
740 vasculature (CD31, grey) and neutrophils (Ly6G, red) as well as probes for ROS (orange) and RNS
741 (yellow). 5 minutes timelapse series were acquired and neutrophils were tracked using Imaris software.

742 **Video 2: CD18 modulates lung neutrophil motility in an intravenous transplant model of KP cells.**

743 Catchup$^{IVM\text{-}red}$ mice were IV injected with KP cells stained with cellTrace dyes (yellow) and either
744 isotype control antibody, CD18 blocking antibody (GAME-46) or CD18 activating antibody (M18/2). 30
745 minutes later lungs were taken for live *ex vivo* confocal microscopy of PCLS. Slices were stained for
746 DNA (Hoechst, blue), vasculature (CD31, grey), neutrophils (Ly6G, purple) and CD45 (cyan). 40
747 minutes timelapse series were acquired, and neutrophils were tracked using Imaris software.

748 **Video 3: ICAM-1 modulates lung neutrophil motility in an intravenous transplant model of KP**
749 **cells.**

750 Catchup$^{IVM\text{-}red}$ mice were IV injected with KP cells stained with cellTrace dyes (yellow) and either
751 isotype control antibody or ICAM-1 blocking antibody. 30 minutes later lungs were taken for live *ex vivo*
752 confocal microscopy of PCLS. Slices were stained for DNA (Hoechst, blue), vasculature (CD31, grey),
753 neutrophils (Ly6G, purple) and CD45 (cyan). 8 minutes timelapse series were acquired, and neutrophils
754 were tracked using Imaris software.

755 **Video 4: CD18 modulates lung neutrophil motility in tumour bearing mice.**

756 Lungs from 10-15 mm KP tumour bearing Catchup$^{IVM\text{-}red}$ mice were harvested for live *ex vivo*
757 multiplexed confocal microscopy of PCLS and stimulated *ex vivo* with either isotype control antibody or
758 CD18 activating antibody (M18/2). Slices were stained for DNA (Hoechst, blue), vasculature (CD31,
759 grey), neutrophils (Ly6G-td Tomato, purple), T-cells (CD8, green), alveolar macrophages (CD11c,
760 orange) and leukocytes (CD45, cyan). 30 minutes timelapse series were acquired, and neutrophils were
761 tracked using Imaris software.

762 **Video 5: G-CSF treatment modulates lung neutrophil motility in a CD18 dependent manner.**

763 Lungs from G-CSF treated mice were harvested for live *ex vivo* multiplexed confocal microscopy of
764 PCLS and stimulated *ex vivo* with either isotype control antibody or CD18 activating antibody (M18/2).
765 Slices were stained for DNA (Hoechst, blue), vasculature (CD31, grey) and neutrophils (Ly6G, purple).
766 15 minutes timelapse series were acquired, and neutrophils were tracked using Imaris software.

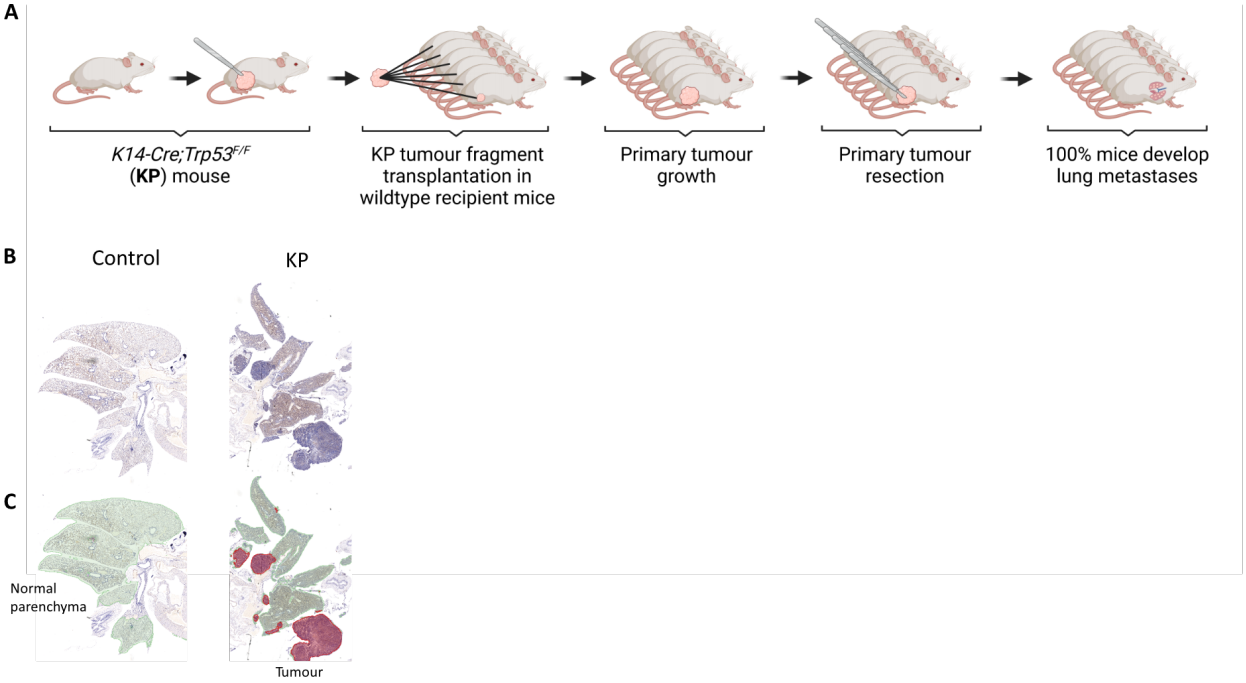

Figure S1: Spontaneous metastasis model.

A) Mammary tumour fragments from KP mice were orthotopically transplanted into WT recipient mice, allowed to grow, then surgically resected when tumour reached 10 mm in any direction. Metastases develop in 100% of recipient mice.

B) Representative hematoxylin & eosin staining from non-transplanted control and metastatic lungs.

C) Annotation showing normal parenchyma (green) and tumour tissue (red) from a pixel classification in QuPath[45].

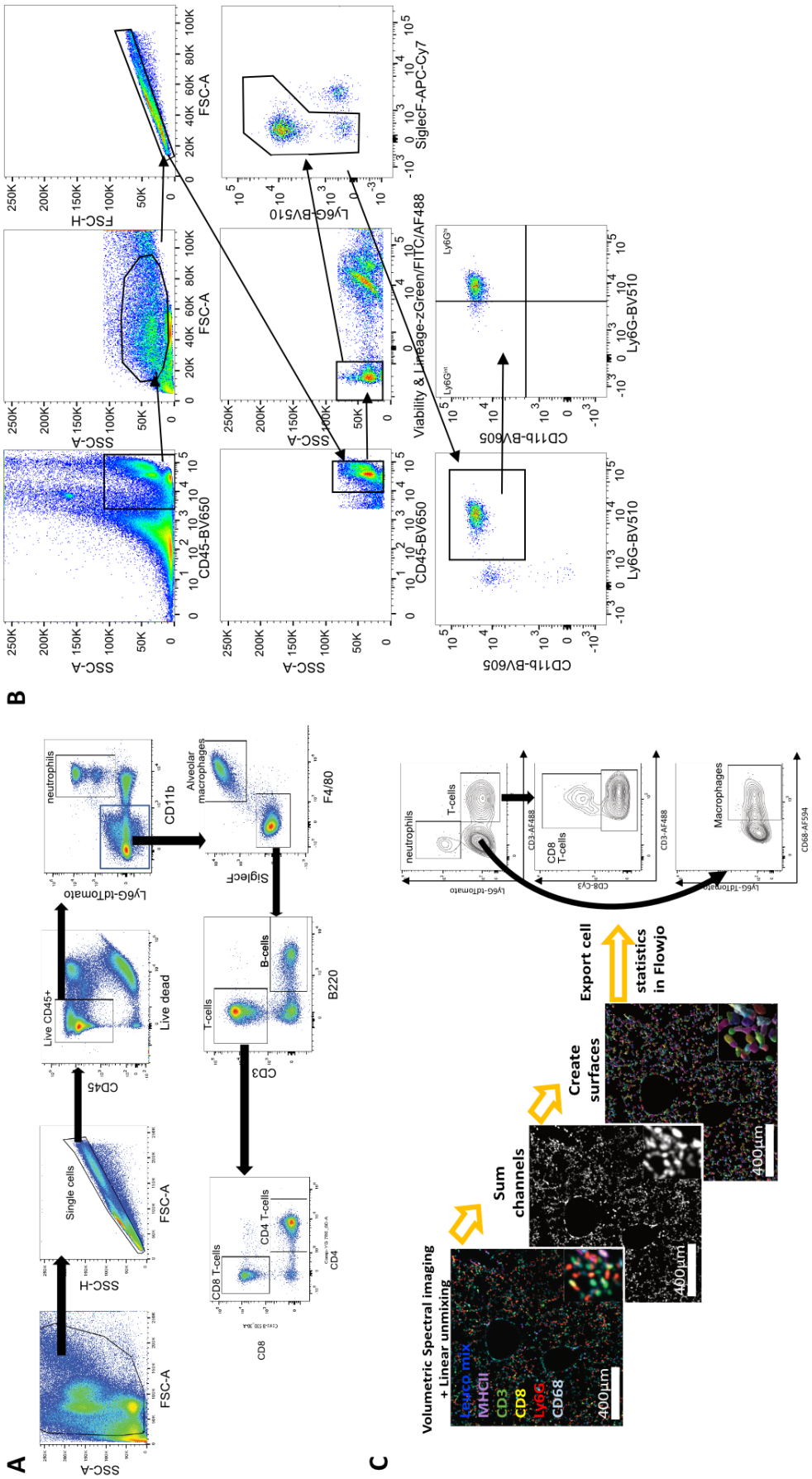

Figure S2: Gating strategies for flow cytometry and Histocytometry.

A) Gating strategy for flow cytometry analysis of dissociated lung to phenotype CD45+ immune cell populations using lung immunophenotyping panel: Neutrophils (CD11b+ Ly6G+), Alveolar macrophages (CD11b- SiglecF+), B- cells (B220+), CD8 T-cells (CD3+ CD8+) and CD4 T-cells (CD3+ CD4+). Relevant to Figure 1.

B) Gating strategy for flow cytometry analysis of $Ly6G^{int}$ and $Ly6G^{hi}$ neutrophil numbers, CD18, CD62L and CD101 neutrophil surface expression in Figures 1, 2 and 3 using neutrophil phenotyping panel.

C) Histocytometry strategy for analysing lung tissue images in Figure 1E-G (Data shown here is the same image from Figure 1E for illustrative purposes). Fixed precision cut lung slices (PCLS) were stained with fluorescently labelled antibodies and imaged with a spectral confocal microscope. After linear unmixing of the different fluorophores, the channels corresponding to the different immune markers were summed to allow the segmentation of all immune cells in Imaris software. Cell statistics were then imported into FlowJo for analysis.

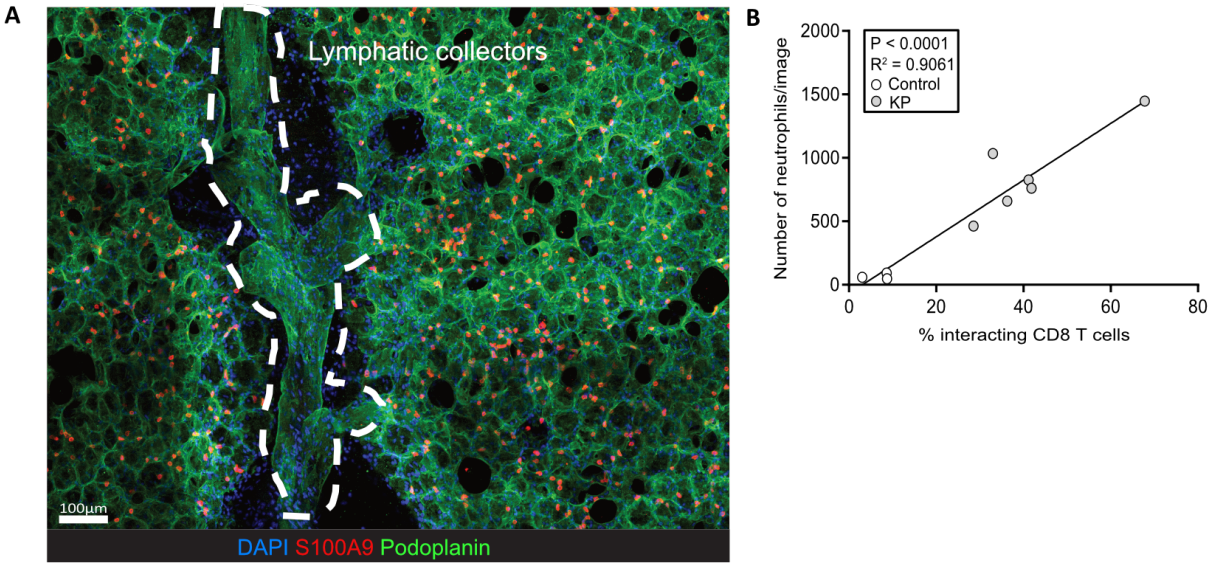

Figure S3: Localisation of lung neutrophils and CD8 T-cells interactions.

(A) Podoplanin (green) staining for lymphatic collectors (it also stains alveolar cells in the lung) in a PCLS from a KP tumour bearing FVB/N mouse. S100A9 (red) was used to stain neutrophils and DAPI (blue) was used to stain DNA.

(B) The correlation between $CD8^+$ T cell:neutrophil interaction and neutrophil numbers was analysed using the Spearman's rank correlation test ($r = 0.8333$ $p=0.0083$); then a linear regression was performed to describe relationship between variables, showing that 90% ($R^2= 0,9061$, $p<0.0001$) of the interactions can be significantly explained by the number of neutrophils in the lung.

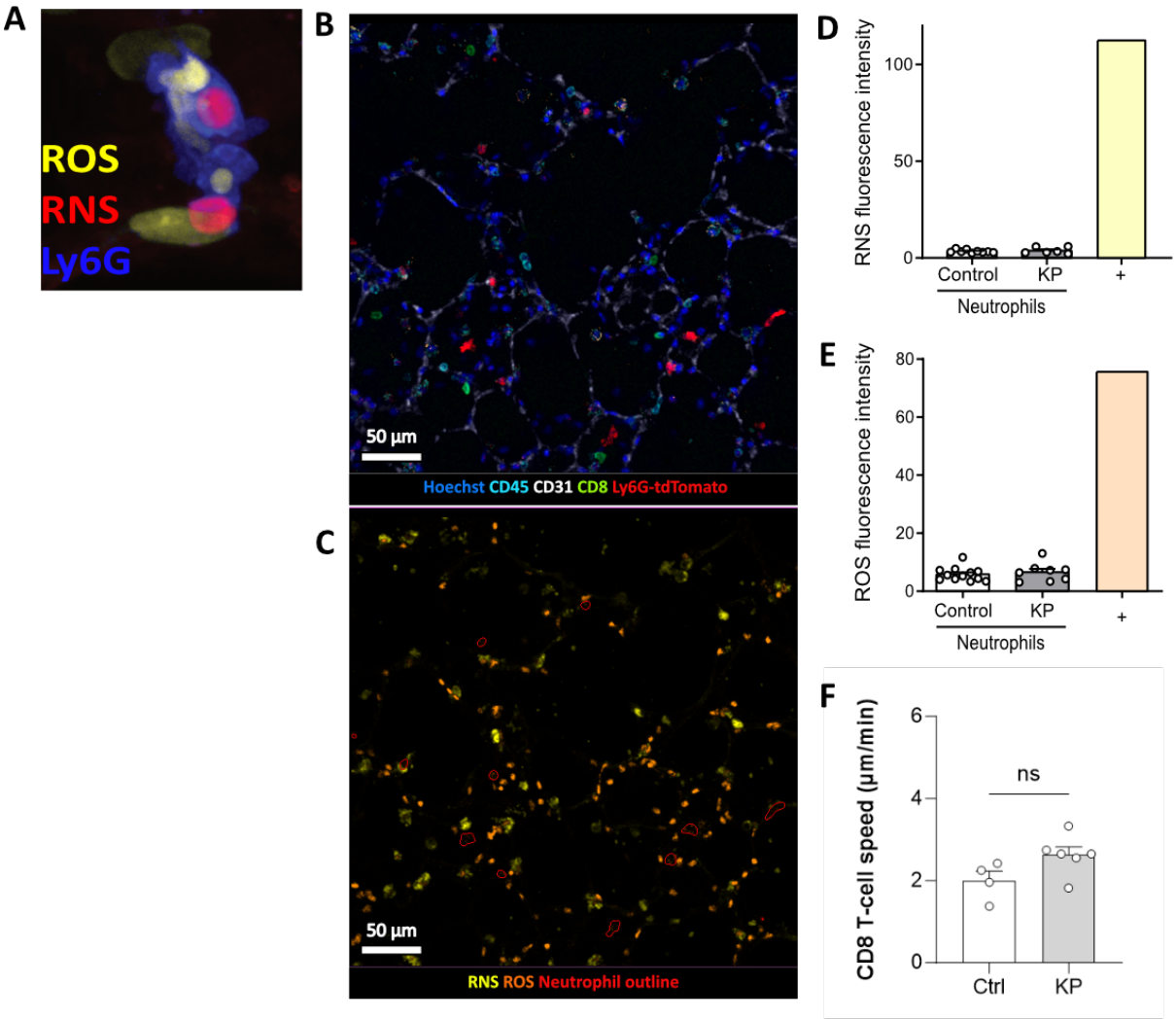

Figure S4: ROS/RNS production in live PCLS and CD8 T-cell speed.

Lungs from control and KP tumour bearing mice were harvested for live *ex vivo* multiplexed confocal microscopy of PCLS to analyse their behaviour and free radical production (Reactive Oxygen Species – ROS and Reactive Nitrogen Species – RNS).

(A) Positive control from a Phorbol 12-myristate 13- acetate (PMA) treated PCLS showing a neutrophil (Ly6G, blue) with cytoplasmic ROS (yellow) and nuclear RNS (red).

(B-C) Slices were stained for DNA (Hoechst, blue), vasculature (CD31, grey), CD8 T-cells (CD8, green), leukocytes (CD45, cyan) and neutrophils (Ly6G, red) as well as probes for ROS (orange) and RNS (yellow).

(D) Quantification of RNS mean fluorescence intensity in neutrophils. The + bar represents the mean intensity from a surrounding RNS positive cell.

(E) Quantification of ROS mean fluorescence intensity in neutrophils. The + bar represents the mean intensity from a surrounding ROS positive cell.

(D-E) Results are expressed as mean ± SEM of n = 8-12 mice per group.

823 (F) CD8 T-cells mean speed in Control and KP orthotopic tumour-bearing mouse lung slices. Results
824 are expressed as mean ± SEM of n = 4 control mice and 6 KP-bearing mice. A parametric T-test was
825 performed, ns $p>0.05$.

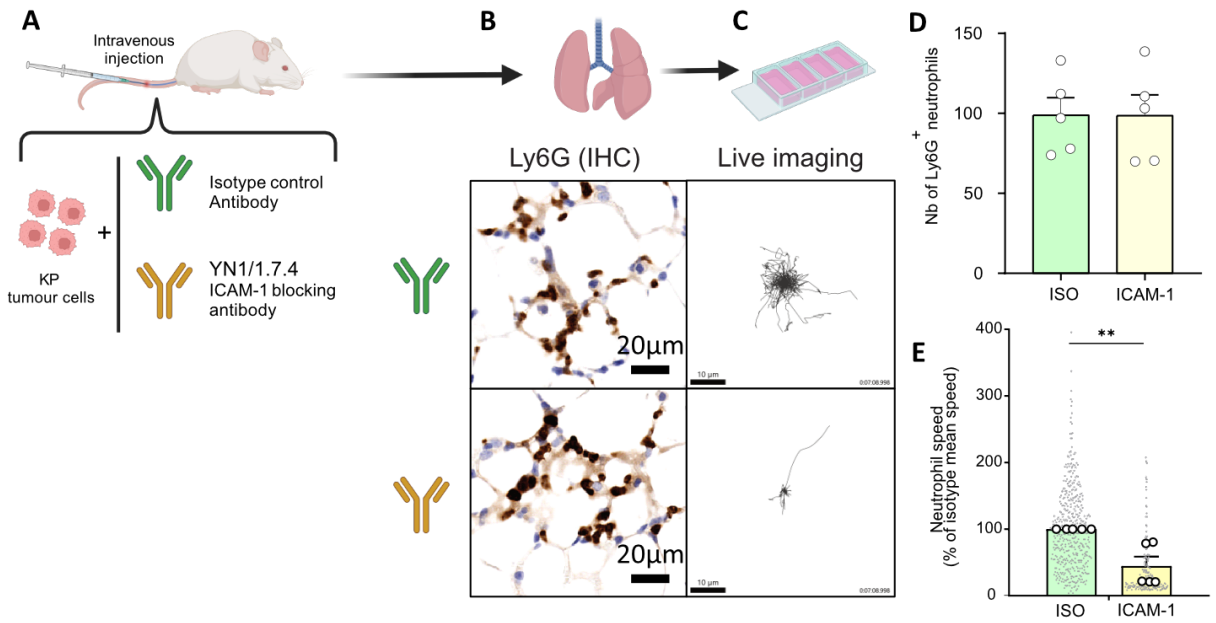

Figure S5: Modulation of neutrophil motility in an intravenous (IV) transplant model of KP cells, using ICAM-1 blocking antibodies.

(A) Schematic of the experiment design. Mice were IV injected with KP cells and either isotype control antibody (green) or ICAM-1 blocking antibodies (yellow). 30 minutes later lungs were taken for live *ex vivo* confocal microscopy of PCLS (see video S3) and Immunohistochemistry.

(B) Representative IHC images from the two treatment groups.

(C) Representative neutrophil tracking plots from the two treatment groups.

(D) Quantification of the number of neutrophils/mm^2 in lung IHC images. Results are expressed as mean ± SEM of 5 mice per group. A T-test was performed.

(E) Quantification of neutrophil speed as a % of the isotype control mean speed from live *ex vivo* microscopy. Grey dots represent the speed of each individual neutrophil (a total of 213-459 tracks per group were analysed) while white dots represent the mean neutrophil speed per mouse. Statistical analysis (nonparametric Mann-Whitney test) was performed on the mean value per animal. Results are expressed as mean ± SEM of n = 5 mice per group. **$p \leq 0.01$.

842

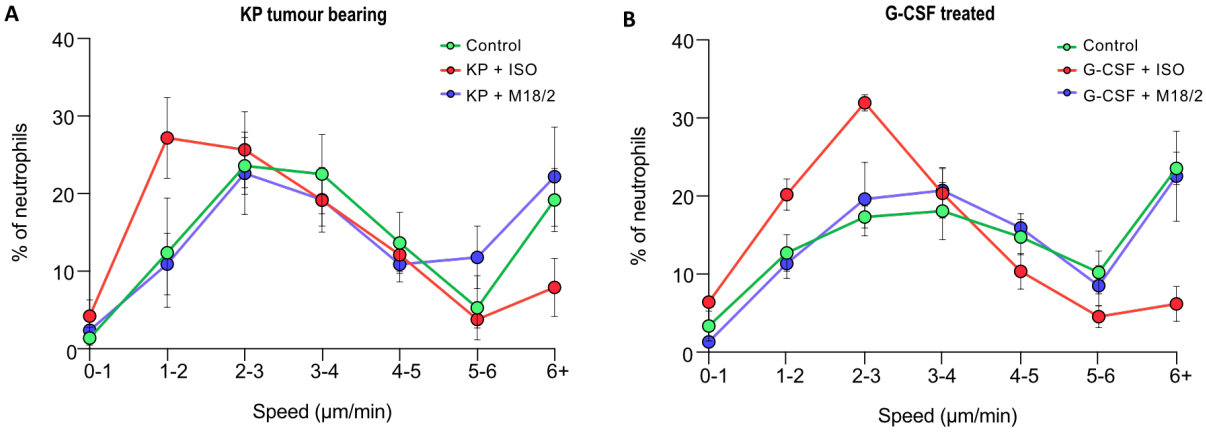

843

844 **Figure S6: Neutrophil speed distribution in the lungs of mice with KP tumour and mice treated**
845 **with G-CSF.**

846 Neutrophils were tracked in live multiplexed confocal microscopy timelapse images of *ex vivo* PCLS
847 after *ex vivo* stimulation with either isotype control antibody or M18/2.

848 (A) Speed distribution of neutrophils from control and KP tumour-bearing mice from Figure 2M. Results
849 are expressed as mean +/- SEM of n = 4 control mice and 6 KP-tumour bearing mice

850 (B) Speed distribution of neutrophils from PBS and G-CSF treated mice from Figure 3E. Results are
851 expressed as mean +/- SEM of n = 4 PBS control and 5 G-CSF treated mice.

852